PNAS Nexus, 2024, 3, 1–11
https://doi.org/10.1093/pnasnexus/pgae044
Advance access publication 27 February 2024
Research Report

Dynamics of nanocluster aerosol in the indoor atmosphere during gas cooking

Satya S. Patra[a,b], Jinglin Jiang[a,b], Xiaosu Ding[a], Chunxu Huang[a,b], Emily K. Reidy[c], Vinay Kumar[d], Paige Price[d], Connor Keech[e], Gerhard Steiner[f], Philip Stevens[c,d], Nusrat Jung[a,*] and Brandon E. Boor[a,b,*]

[a]Lyles School of Civil Engineering, Purdue University, West Lafayette, IN 47907, USA
[b]Ray W. Herrick Laboratories, Center for High Performance Buildings, Purdue University, West Lafayette, IN 47907, USA
[c]Department of Chemistry, Indiana University, Bloomington, IN 47405, USA
[d]O'Neill School of Public and Environmental Affairs, Indiana University, Bloomington, IN 47405, USA
[e]DURAG Inc., Minnetonka, MN 55343, USA
[f]GRIMM Aerosol Technik Ainring GmbH & Co. KG, Ainring 83404, Germany
*To whom correspondence should be addressed: Email: nusratj@purdue.edu (N.J.); Email: bboor@purdue.edu (B.E.B.)
Edited By: Vicki Grassian

Abstract

Nanocluster aerosol (NCA: particles in the size range of 1–3 nm) are a critically important, yet understudied, class of atmospheric aerosol particles. NCA efficiently deposit in the human respiratory system and can translocate to vital organs. Due to their high surface area-to-mass ratios, NCA are associated with a heightened propensity for bioactivity and toxicity. Despite the human health relevance of NCA, little is known regarding the prevalence of NCA in indoor environments where people spend the majority of their time. In this study, we quantify the formation and transformation of indoor atmospheric NCA down to 1 nm via high-resolution online nanoparticle measurements during propane gas cooking in a residential building. We observed a substantial pool of sub-1.5 nm NCA in the indoor atmosphere during cooking periods, with aerosol number concentrations often dominated by the newly formed NCA. Indoor atmospheric NCA emission factors can reach up to ~10^{16} NCA/kg-fuel during propane gas cooking and can exceed those for vehicles with gasoline and diesel engines. Such high emissions of combustion-derived indoor NCA can result in substantial NCA respiratory exposures and dose rates for children and adults, significantly exceeding that for outdoor traffic-associated NCA. Combustion-derived indoor NCA undergo unique size-dependent physical transformations, strongly influenced by particle coagulation and condensation of low-volatility cooking vapors. We show that indoor atmospheric NCA need to be measured directly and cannot be predicted using conventional indoor air pollution markers such as $PM_{2.5}$ mass concentrations and NO_x ($NO + NO_2$) mixing ratios.

Keywords: atmospheric aerosol, air pollution, nanoparticles, aerosol exposure, particulate matter

Significance Statement

In contrast to the outdoor atmosphere, the dynamics of nanocluster aerosol (NCA: 1–3 nm) in indoor atmospheric environments remains poorly characterized. We report significant formation of NCA down to 1 nm during indoor gas cooking. Our measurements reveal that indoor atmospheric NCA undergo size-dependent transformations at rates remarkably different from those observed outdoors. We found that during gas cooking, indoor NCA can be present at concentrations (1–10 million NCA/cm^3) much greater than in traffic-influenced areas despite their fast coagulation and diffusional deposition. The large NCA pool results in a significant respiratory burden for children and adults. Our results demonstrate that indoor NCA must be considered as a distinct air pollutant category that should be routinely monitored when evaluating aerosol emissions.

Introduction

Atmospheric nanocluster aerosol (NCA) are nano-sized molecular clusters that are from 1 to 3 nm in diameter and represent a critical interface in the formation and growth of new atmospheric particles from gas-phase precursors (1–3). In contrast to larger atmospheric aerosol particles, NCA are not routinely measured in ambient air due to analytical challenges, including low particle-counting accuracy, significant deposition losses of NCA in the measuring instrument, and the complexity of accurately classifying and detecting nano-sized particles (4). Recent advancements in electrical mobility-based measurement techniques for sub-10 nm particles, along with the development of particle size magnifying methods, have enabled the accurate sizing and detection of clusters as small as around 1 nm (5). Prior measurements of outdoor atmospheric

Competing Interest: G.S. is a full-time employee of GRIMM Aerosol Technik Ainring GmbH & Co. KG, which has a potential direct or indirect financial interest in the subject matter discussed in the manuscript. C.K. is a full-time employee of DURAG Inc., which has a potential direct or indirect financial interest in the subject matter discussed in the manuscript.
Received: August 25, 2023. **Accepted:** January 16, 2024

NCA have revealed that NCA can persist at high number concentrations (10^3–10^5 cm^{-3}) due to direct emissions from traffic and nucleation of sulfuric acid and low-volatility organic vapors (2, 3, 6, 7). Inhalation exposure to the newly formed NCA is also of concern. NCA efficiently deposit in the respiratory system (1). When inhaled, NCA have a significantly higher deposition fraction in the upper respiratory tract than other sub-100 nm ultrafine particles (8), and once deposited, they can move between cells and enter the bloodstream (9), potentially translocating to organs such as the liver and brain (10, 11). Furthermore, NCA exhibit high deposition in the tracheobronchial region of the lungs, with the tracheobronchial deposition fraction reaching a maximum near the NCA size fraction (~4 nm) (1). Due to their high surface area-to-volume ratios (Fig. S1) (12), NCA are associated with a heightened propensity for bioactivity and adverse cytotoxic, apoptotic, and proinflammatory effects in eukaryotic and endothelial cells (13–15). Despite recent efforts to characterize outdoor atmospheric NCA, little is known regarding NCA dynamics and exposures in indoor environments, where people spend about 90% of their time (16).

The indoor atmosphere is uniquely different from that outdoors. Many aspects of buildings and their occupants are likely to influence the prevalence and behavior of indoor atmospheric NCA. Factors that affect the indoor production and loss of NCA are expected to differ from those outdoors. Given the nature of human activities in indoor spaces, NCA sources are likely to be highly transient, with concentrations changing rapidly over short timescales (1). In contrast to outdoor air, the indoor atmosphere is characterized by minimal dilution due to poor building ventilation and significant potential for NCA–surface interactions due to the substantial surface area of occupied buildings (17). A few observational studies have identified indoor sources of NCA, including NCA nucleation following the ozonolysis of monoterpenes and skin oil (1, 18) and direct NCA emissions during 3D printing and cooking (19–21). However, a complete mechanistic understanding of the formation and transformation of indoor atmospheric NCA down to 1 nm in residential buildings is presently lacking.

Combustion processes are known to generate sub-10 nm nanoparticles (22). Field measurements at natural gas-burning plants have reported elevated concentrations (>10^5 cm^{-3}) of particles between 2 and 7 nm (23). On the contrary, particle emissions from conventional and condensing boilers used in residential heating systems, fueled by natural gas and liquefied petroleum gas (LPG), exhibit a primary particle mode between 10 and 20 nm (24). Other combustion sources, such as diesel and natural gas engines, have been shown to emit NCA ranging from ~10^{12} to >10^{15} NCA/kg-fuel (Table S7). Here, we report that indoor atmospheric NCA emitted during propane gas cooking can be present at number concentrations (10^5–10^7 cm^{-3}) that far exceed those observed at traffic-influenced urban outdoor sites despite their tendency to coagulate and diffuse to surfaces. Indoor NCA emission factors were similar to or greater than those for vehicles with gasoline and diesel engines (Table S7). Our measurements reveal that NCA emitted during propane gas cooking undergo rapid size-dependent transformations driven by high rates of inter- and intramodal coagulation. Thus, NCA emitted indoors during propane-gas-stove combustion are subject to rapid physical transformations. Lastly, we demonstrate how high NCA emissions from gas cooking cause a major respiratory burden for children and adults due to large doses of NCA to the head airways and tracheobronchial region. Our results are broadly relevant given the widespread use of gas combustion (propane, methane) for indoor cooking by the global population (25–27); thus, indoor NCA exposures may represent a major public health concern.

The observations reported here are based on a measurement campaign conducted in the Purdue zero Energy Design Guidance for Engineers (zEDGE) test house. Indoor NCA number size distributions were measured in real-time using a novel high-resolution particle size magnifier—scanning mobility particle sizer (PSMPS). Our PSMPS measurements were coupled with the aerosol general dynamic equation (GDE) to provide fundamental insights into the size-dependent (d_p) behavior of NCA in indoor atmospheres (28, 29). To facilitate direct comparisons with other NCA sources, we present NCA production terms, including the apparent NCA emission rate ($E_{NCA,app}$, min^{-1}), the NCA emission factor based on a carbon mass basis (E_{NCA}, kg-$fuel^{-1}$), and the NCA coagulation source ($CoagSrc_{dp}$, cm^{-3} s^{-1}), and NCA loss terms, including the NCA coagulation sink ($CoagSnk_{dp}$, s^{-1}) and aerosol Fuchs surface area (A_{Fuchs}, μm^2 cm^{-3}) (20, 29, 30). Our analysis also considers NCA transformations due to condensation of low-volatility cooking vapors, parameterized through size-resolved condensational growth rates ($GR_{Cond,dp}$, nm h^{-1}). Fundamentally, we have parametrized the key physical forces influencing the transformation of indoor atmospheric NCA and shown how such parameters can be used to evaluate how indoor NCA size distributions change and evolve over time. Overall, our field measurement campaign reveals important, and previously unreported, dynamics of sub-3 nm NCA emitted from gas cooking, demonstrating that NCA should be routinely monitored for a more complete assessment of size-dependent indoor nanoparticle dynamics.

Results and discussion

Time and size dependence of the formation and transformation of indoor atmospheric NCA during propane gas cooking

In Fig. 1, we show the time-resolved evaluation of indoor atmospheric NCA formation and transformation during propane gas cooking via high-resolution online nanoparticle measurements from 1.18 to 3 nm with a PSMPS. We compare NCA dynamics for gas cooking experiments involving boiling water (left) and cooking grilled cheese (right; Fig. S9 shows the same for cooking buttermilk pancakes). In Figs. 2 and 3, we evaluate the relationship between indoor atmospheric NCA source and loss processes during active propane-gas-combustion periods for all these experiments. The results revealed the presence of a large pool of NCA in the indoor atmosphere during propane gas combustion for indoor cooking. The PSMPS utilized a new differential mobility analyzer (DMA) that enabled high-size- and time-resolved NCA monitoring; this improved the characterization of episodic indoor NCA production events such as those observed here. We detected very high number concentrations of indoor atmospheric NCA (N_{NCA}) during propane gas cooking, ranging from ~10^5 to 10^7 cm^{-3}, far exceeding those reported at urban and rural outdoor sites (Table S6).

Fig. 1 also represents the first reporting of CoagSrc, CoagSnk, and A_{Fuchs} for indoor atmospheric NCA emitted from propane gas cooking. All three are key parameters defining how NCA number size distributions transform due to coagulation among smaller molecular clusters (CoagSrc) and intermodal coagulation with larger aerosol particles in the Aitken and accumulation modes (CoagSnk, A_{Fuchs}). The net difference between CoagSnk and CoagSrc is also reported ($CoagSnk_{Net}$, s^{-1}; Eq. 5) (29). The boiling water experiments can be categorized as small/moderate CoagSnk cases, based on the values of A_{Fuchs} and $CoagSnk_{Net}$. Similarly, cooking buttermilk pancakes and grilled cheese can be classified as large CoagSnk cases. The latter was due to the release of significant quantities of larger atmospheric aerosol particles between 10 and 1,000 nm from high

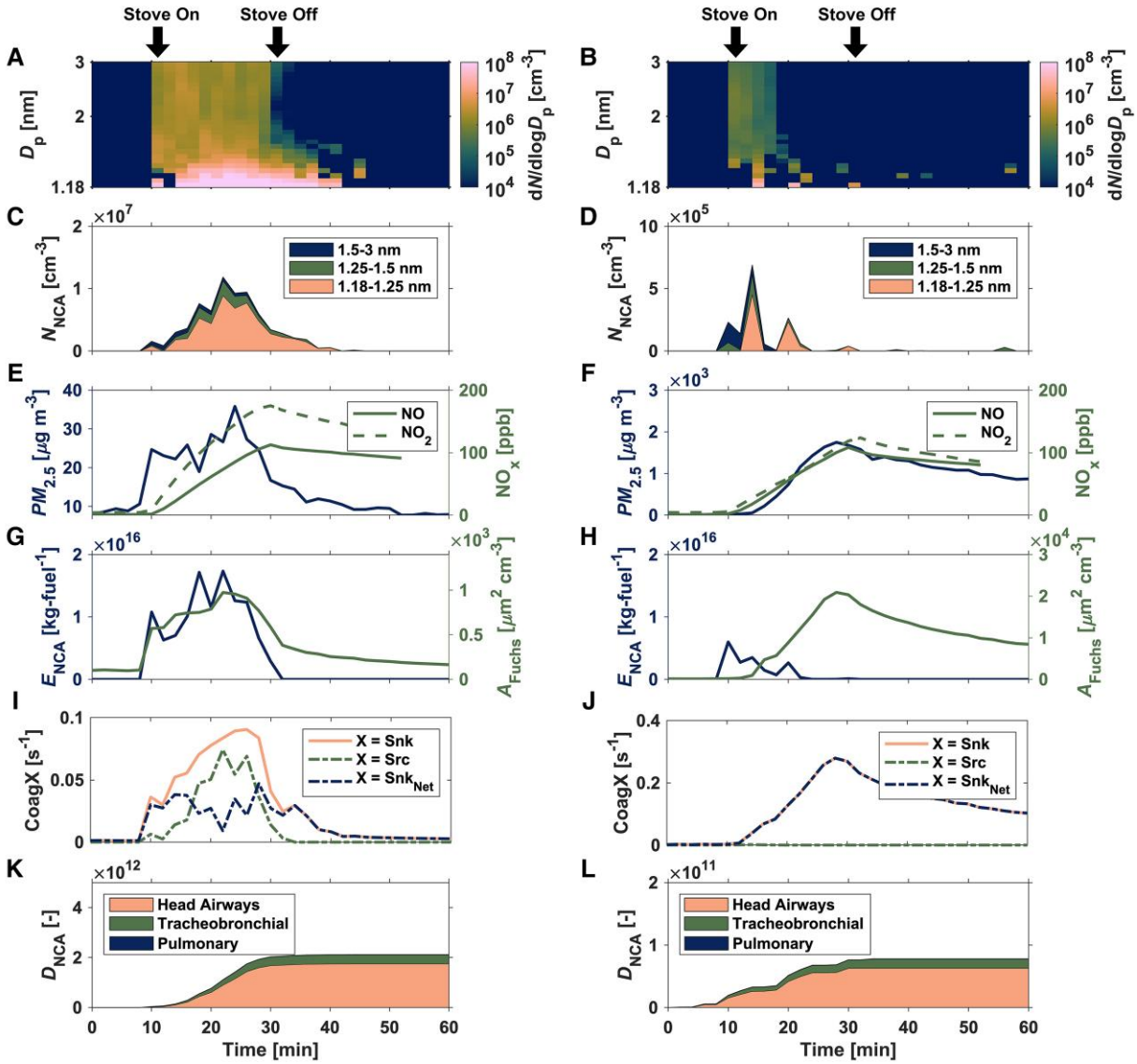

Fig. 1. Time-resolved evaluation of indoor atmospheric NCA formation and transformation during propane gas cooking via high-resolution online nanoparticle measurements—first row: propane-gas-cooking-emitted NCA number size distributions ($dN/dlogD_p$); second row: size-integrated (1.18–3 nm) propane-gas-cooking-emitted NCA number concentrations (N_{NCA}); third row: Conventional indoor air pollution markers: $PM_{2.5}$ mass concentrations and NO + NO_2 mixing ratios; fourth row: carbon-mass-based (1.18–3 nm) propane-gas-cooking-emitted NCA emission factors (E_{NCA}) and the aerosol Fuchs surface area (A_{Fuchs}); fifth row: coagulation sink, coagulation source, and the net difference between the coagulation sink and coagulation source; and sixth row: cumulative adult respiratory-tract-deposited doses (D_{NCA}) during the propane-gas-cooking measurements in the Purdue zEDGE test house. Left: A, C, E, G, I, K): composite median of small/moderate indoor CoagSnk cases (boiling water). Right: B, D, F, H, J, L): composite median of large indoor CoagSnk cases (cooking grilled cheese; composite median for cooking buttermilk pancakes is shown in the supplementary material, Fig. S9). The coagulation sink presented in I) and J) represents the median of the size-resolved coagulation sink values in the NCA size fraction. For X = Src in I) and J), the coagulation source values are computed as the median of $CoagSrc_{dp}/N_{dp}$ over the NCA size fraction.

temperature butter-based cooking processes (Figs. 4 and S8); this increased the NCA coagulation scavenging potential of the indoor atmosphere (Fig. 1). Our measurements reveal that NCA can be present in indoor air for the duration of the gas combustion process, or until rates of intermodal coagulation scavenging exceed those for heavily polluted urban atmospheres (Figs. 1 and 2). Thus, NCA were observed to remain in the indoor atmosphere for the entire active combustion period when the background aerosol concentrations were low, such as during the boiling water experiments. However, NCA concentrations declined sharply during cooking experiments once the generation of larger cooking-associated particles began. This shift drove the coagulation potential values of the indoor atmospheric environment to levels similar to those in heavily polluted outdoor environments, thereby scavenging the NCA. Quantitatively, when CoagSnk and A_{Fuchs} levels during cooking exceed those found in heavily polluted outdoor air ($CoagSnk_{Net}$ >0.2 s^{-1} and A_{Fuchs} >10^4 μm^2 cm^{-3}), N_{NCA} and E_{NCA} start to decrease (Figs. 1 and 2). This unique NCA transformation becomes apparent 6 min after butter-based cooking begins, as illustrated in Figs. 1 (right) and S10. A sudden increase in CoagSnk and A_{Fuchs} is noticeable at this point. Concurrently, there is a reduction in the prevalence of sub-1.5 nm molecular clusters, with N_{NCA} <10^4 cm^{-3} and E_{NCA} <10^{13} kg-fuel^{-1}. During the active gas combustion period, with small-to-moderate coagulation sinks, the presence of indoor NCA at very high-number concentrations demonstrates that the rate of NCA production often exceeds that of NCA loss, creating a major

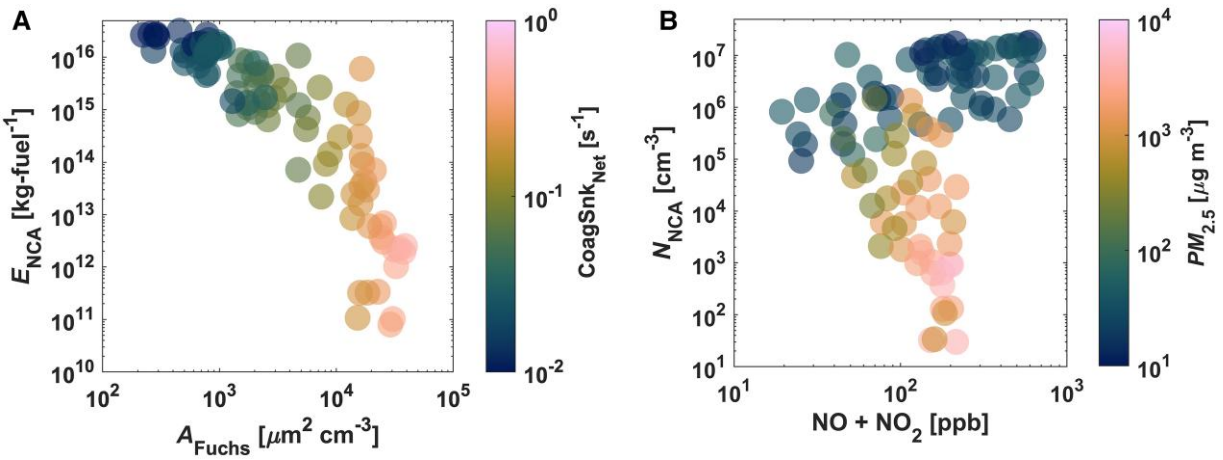

Fig. 2. Dynamics of combustion-derived NCA in the indoor atmospheric environment during gas cooking. A) Relationship between the propane-gas-cooking-emitted NCA emission factor (E_{NCA}) and coagulation scavenging parameters, the aerosol Fuchs surface area (A_{Fuchs}) and net coagulation sink ($CoagSnk_{Net}$), during the gas-stove-combustion period. The color of the markers represents $CoagSnk_{Net}$. B) Relationship between size-integrated (1.18–3 nm) propane-gas-cooking-emitted NCA number concentrations (N_{NCA}) and conventional indoor air pollution markers, $PM_{2.5}$ mass concentrations, and NO + NO_2 mixing ratios, during the gas-stove-combustion period. The color of the markers represents the $PM_{2.5}$ mass concentrations.

NCA respiratory burden for occupants. This relationship is illustrated in Fig. 3 as size-resolved indoor NCA source and loss terms between 1.18 and 3 nm.

Indoor atmospheric NCA formation and transformation processes during propane gas cooking are highly transient, with NCA number size distributions and concentrations changing rapidly while the stove was in use (Fig. 1). Such time-dependent changes are in contrast to outdoor observations of NCA, where the abundance of NCA often changes much more slowly during atmospheric nucleation events (3). Immediately following the initiation of the propane-gas-combustion event, we observed indoor NCA number concentrations (N_{NCA}) to increase from background levels of ~10^2 to ~10^5–10^6 cm^{-3}. N_{NCA} rose to ~10^7 cm^{-3} shortly thereafter. Particle number size distributions ($dN/d\log D_p$) exhibited strong size-dependency in the NCA size range, with a significant fraction of the indoor NCA population found below 1.5 nm (Figs. 1, 3, and S8). Our measurements show that freshly nucleated NCA from 1.18 to 1.5 nm are present in the indoor atmosphere for the entirety of the 20 min propane-gas-cooking period during experiments with small-to-moderate coagulation sinks. The detected NCA are likely flame-generated incipient soot particles (33–36), also referred to as nanoparticles of organic carbon (NOC), composed of fullerenes, graphene, and partially matured NOC (37–39).

The measured indoor NCA size distributions during propane gas cooking are the result of the balance between NCA production and loss processes, as defined in the aerosol GDE (Eqs. 1 and 2). The temporal evolution of both is presented in Fig. 1, and their size-dependency is shown in Fig. 3. These include the size-integrated NCA production terms—the NCA apparent emission rate ($E_{NCA,app}$, min^{-1}), NCA emission factor (E_{NCA}, kg-fuel^{-1}), and NCA coagulation source (CoagSrc, cm^{-3} s^{-1}), and the size-integrated NCA loss terms—the NCA coagulation sink (CoagSnk, s^{-1}) and aerosol Fuchs surface area (A_{Fuchs}, μm^2 cm^{-3}). E_{NCA} fluctuated during the active propane-gas-combustion period (Fig. 1) and was generally between 10^{14} and >10^{16} kg-fuel^{-1} for small-to-moderate coagulation sink cases (Fig. 2). The apparent rate of formation of NCA increased with decreasing particle diameter, with the highest emission rates reported for NCA between 1.18 and 1.5 nm (Fig. 3). 10^{13}–10^{16} NCA are typically released into the indoor atmosphere during a single 20-min propane-gas-cooking event. Such substantial formation of indoor nanoparticles cannot be observed when using conventional aerosol instrumentation that cannot accurately size classify and detect sub-1.5 nm NCA.

Our PSMPS measurements demonstrate that the NCA emission factor and the apparent rate of formation of NCA are inversely correlated with the coagulation scavenging potential of the indoor atmosphere (Figs. 2, 3, and S11). This relationship has previously been demonstrated for NCA during new particle formation events in outdoor environments (30, 40). However, suppression of outdoor new particle formation events was observed when A_{Fuchs} values exceeded 200 μm^2 cm^{-3} (30). In our propane-gas-combustion experiments, we observed very high NCA formation rates, which significantly offset the suppression A_{Fuchs} values by an order of magnitude. Therefore, interactions between newly formed indoor NCA and larger aerosol particles must be considered to accurately model the airborne fate and transport of molecular clusters down to 1 nm. As shown in Fig. 3, CoagSnk is a significant contributor to the size-resolved apparent emission rates; its magnitude relative to all terms in the aerosol GDE (Eqs. 1 and 2) can range from about 50 to 92%. To ensure accurate modeling of indoor NCA emissions, it is crucial to accurately model the interaction of NCA with larger aerosol particles. Equally important is modeling the self-coagulation among smaller molecular clusters.

Coagulation among smaller molecular clusters significantly alters the dynamics of the nanoparticle population emitted from vehicle engine exhaust (41, 42). We demonstrate a similar effect for the first time during indoor cooking. Our PSMPS results during propane gas cooking, particularly in small-to-moderate CoagSnk cases, show that intramodal coagulation can contribute up to 40% to the size-resolved NCA dynamics (Fig. 3C, top panel). Surprisingly, the ventilation and deposition terms in the aerosol GDE had a negligible impact on the size-resolved apparent emission rate calculation. The median $CoagSnk_{Net}$ value across all propane-gas-cooking experiments was 400 h^{-1}, which is significantly higher than both the median deposition rate (1.3 h^{-1}) and the outdoor air ventilation rate (0.45 h^{-1}). Therefore, as shown in Fig. 3, indoor NCA transformations are much more sensitive to CoagSrc, CoagSnk, and dN/dt values than the ventilation rate and indoor surface deposition loss rate coefficient (Eq. 2).

Condensation of low volatility organic compounds (LVOCs) and semi-volatile organic compounds (SVOCs) is an important physical process affecting size-resolved NCA particle dynamics for

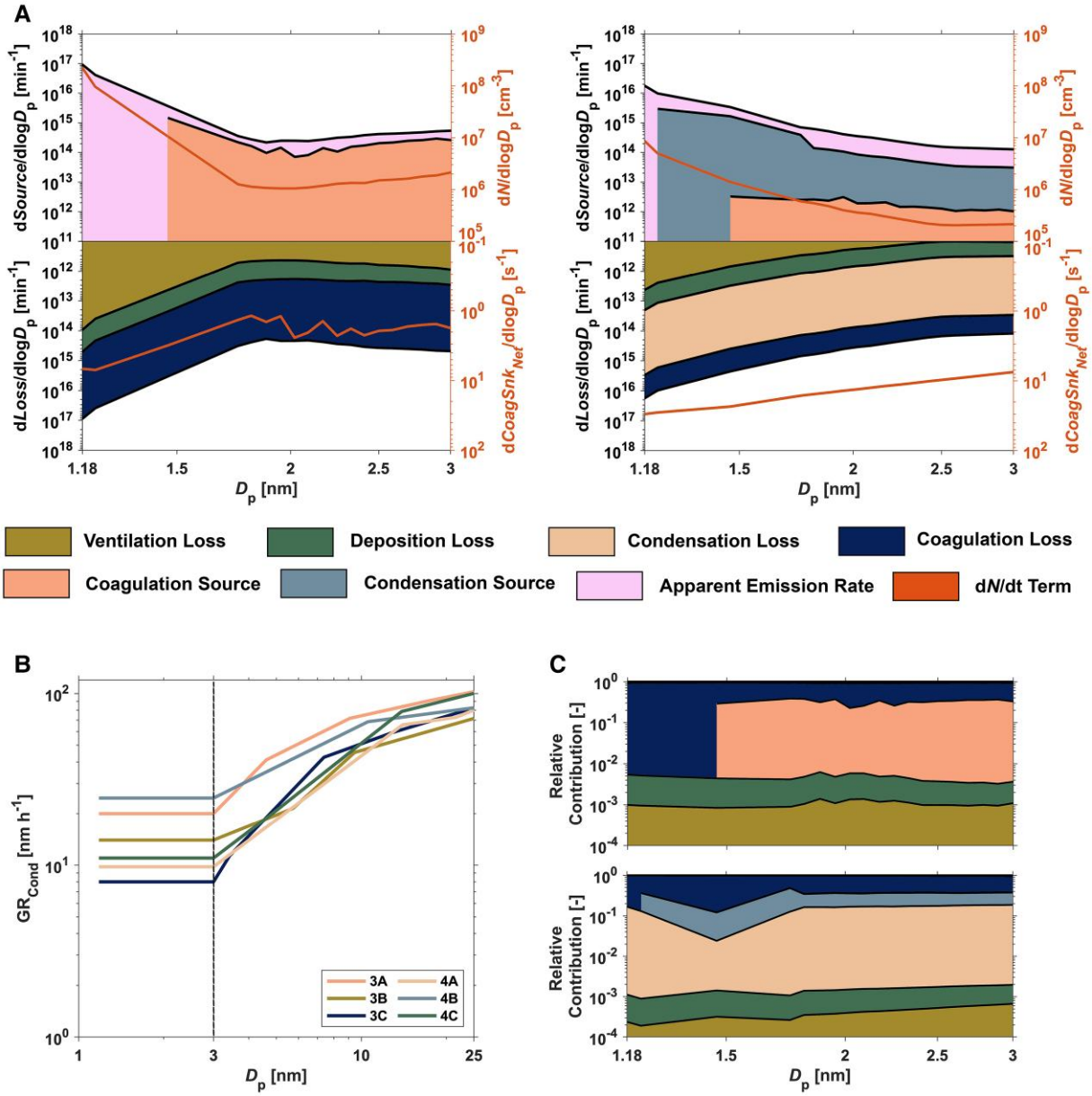

Fig. 3. Size-resolved evaluation of combustion-derived NCA dynamics in the indoor atmospheric environment during propane gas cooking. A) The apportionment of NCA source terms (apparent emission rate, coagulation source, and condensation source) and NCA loss terms (ventilation loss, deposition loss, coagulation loss, and condensation loss). The coagulation source region in this plot is computed as the product of $CoagSrc_{dp}$ and the volume of the Purdue zEDGE test house. The ventilation loss, deposition loss, coagulation loss, condensation loss, and condensation source are also computed as the product of Eqs. S7, S8, S9, S14 ($Cond_{(d_{p,i})}$), and S14 ($Cond_{(d_{p,i-1})}$) and the volume of the Purdue zEDGE test house, respectively. These plots also present the cooking-emitted NCA number size distributions and $CoagSnk_{Net}$ for the NCA size fraction. The plot on the left presents the mean values across all small/moderate indoor CoagSnk cases and the plot on the right presents the mean values across all large indoor CoagSnk cases. B) The size-resolved condensational growth rate of particles emitted from butter-based propane-gas-stove cooking in the Purdue zEDGE test house. The values to the right of the dashed line in the plot were computed using the methods described in the supplementary material, while the values to the left of the dashed line represent a single-value extrapolation down to 1.18 nm. C) Size-resolved relative contribution of each NCA source term, NCA loss term, and the dN/dt term toward calculation of the apparent emission rate aggregated and averaged over the active propane-gas-combustion periods for (top) small/moderate indoor CoagSnk cases and (bottom) large indoor CoagSnk cases. Each *y*-axis is presented in logarithmic scale. All results for A–C are during the active propane-gas-combustion period of the measurements.

butter-based cooking processes (Fig. 3C, bottom panel). This effect is prominent because fat-based cooking activities emit a wide range of LVOCs and SVOCs that can partition between the gas and particle phases (43, 44). As a result, we observed very high condensational growth rates ($GR_{Cond,dp}$) of particles in the 3–25 nm size range (mean $GR_{Cond,dp} = 48$ nm h^{-1}) during our butter-based propane-gas-cooking measurements, which are 5 to 50 times higher than typical outdoor particle growth rates observed during new particle formation events (ranging from 1 to 10 nm h^{-1} (45)). Additionally, during butter-based cooking measurements, we observe a size-dependent behavior in $GR_{Cond,dp}$, with $GR_{Cond,dp}$ increasing with increasing particle size. This suggests the presence of additional condensable semi-volatile vapors for larger particle sizes. This study is the first to report the inclusion of the condensational growth of particles in the aerosol GDE for indoor cooking processes. It is important to note that

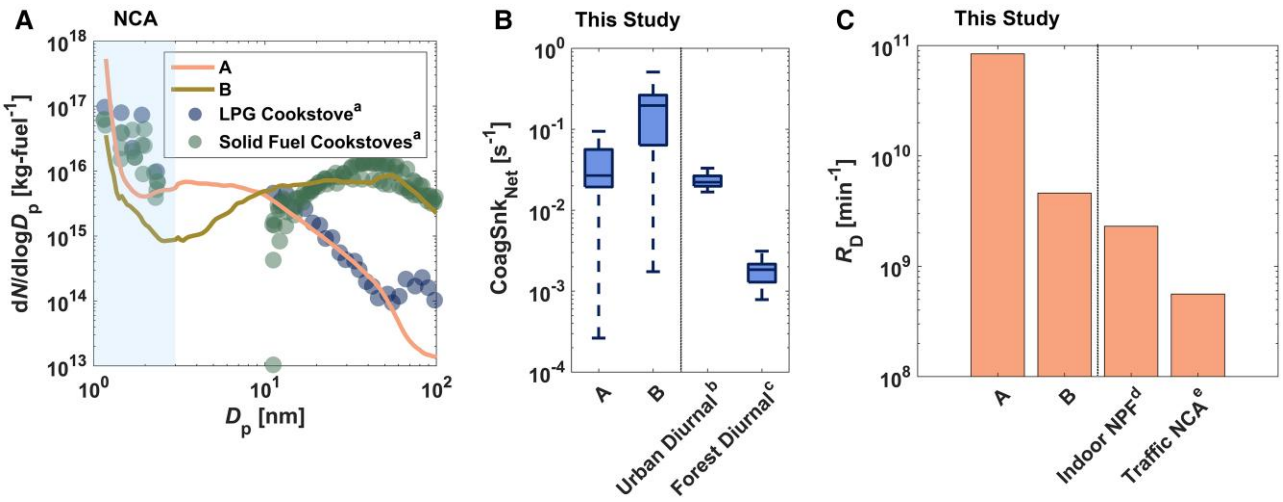

Fig. 4. Comparison with other atmospheric NCA studies: A) mean particle number size distributions ($dN/dlogD_p$) during the active propane-gas-combustion period compared with $dN/dlogD_p$ reported for emissions from a LPG cookstove and solid fuel cookstoves (20); B) net coagulation sink ($CoagSnk_{Net}$) during the active propane-gas-combustion period compared with the diurnal coagulation sink for 1 nm particles reported in the Pearl River Delta of China (Urban Diurnal[b]) (31) and boreal forest (Forest Diurnal[c]) (32); C) size-integrated (1.18–3 nm) NCA respiratory-tract-deposited dose rates ($R_{D,NCA}$) for adults during the active propane-gas-combustion period compared with size-integrated NCA respiratory-tract-deposited dose rates for Indoor NPF[d] (1.2–500 nm) (1) and Traffic NCA[e] (1.2–800 nm) (2). "A" and "B" in the axis labels and legends represent small/moderate and large indoor CoagSnk cases, respectively.

while the condensation of these compounds affects the dynamics of particles in individual-size bins, when integrated over the entire NCA size fraction, the condensation sources and losses (Eq. 2) largely offset each other, resulting in only a minor contribution to the apparent emission rate over the entire size fraction. However, including condensational growth is crucial to understand the dynamics of individual size bins. Thus, modeling the condensation process (including condensation sources and losses) is vital to explain how particles evolve at specific sizes, and these processes tend to cancel each other out when considering the collective particle population dynamics over a wide range of sizes.

Our measurements demonstrate that indoor concentrations of combustion-derived NCA cannot be accurately predicted using conventional and widely used indoor air pollution markers, such as $PM_{2.5}$ mass concentrations and NO_x ($NO + NO_2$) mixing ratios (Fig. 2). While we observed the increase in N_{NCA} to be associated with elevations in $PM_{2.5}$ and NO_x levels (Fig. 1), correlations between N_{NCA} with the two were weak (Figs. S11 and S12). As illustrated in Fig. 2, for a 100-ppb change in NO_x mixing ratios, propane-gas-cooking-emitted NCA number concentrations can vary by over five orders of magnitude. We normalized the apparent emission rates by NO_x mixing ratios (Fig. S13) to show that propane-gas-stove-emitted NCA is not very sensitive to NO_x emissions from propane gas combustion; the NO_x-normalized $E_{NCA,app}$ further generalizes our results. While indoor $PM_{2.5}$ mass concentrations correlate with NCA coagulation scavenging parameters ($CoagSnk_{Net}$, A_{Fuchs}; Fig. S11), they show no significant dependency on N_{NCA} (Pearson coefficient <−0.4; Fig. S12). Our study provides evidence that indoor NCA emitted from propane gas cooking must be measured directly using high-resolution online nanoparticle instrumentation.

Comparison with previous atmospheric NCA studies

We have compared the results of our propane-gas-cooking measurements with those from other atmospheric NCA studies, as illustrated in Fig. 4. The NCA emissions from our propane-gas-cooking measurements were comparable with those reported by Jathar et al. (20) for solid and gas fuel cookstoves (Fig. 4). Additionally, we have compared the emission factors from our propane-gas-cooking measurements with recently published NCA emission factors from exhaust emissions of internal combustion engines and outdoor near-road environments (Table S7). In general, our observed emission factors from propane gas cooking ranged from approximately equal to up to a thousand times greater than those listed in Table S7. Similar emission factors were found for modern diesel engines at higher loads (2, 46) or in proximity to roadways during peak traffic periods (2), thereby highlighting the environmental significance of NCA emissions during indoor propane gas cooking.

Among all propane-gas-combustion measurements, the indoor $CoagSnk_{Net}$ was similar to or greater than that reported for urban outdoor air (Fig. 4). NCA number concentrations during propane gas cooking were only reduced when indoor $CoagSnk_{Net}$ >0.2 s^{-1}; this is about 10-fold greater than that reported for urban air in the Pearl River Delta of China (outdoor $CoagSnk_{Net}$: ~0.02 s^{-1}) (31). Similarly, the indoor aerosol Fuchs surface area during propane gas cooking (indoor A_{Fuchs}: ~10^2–10^4 $\mu m^2\ cm^{-3}$) often exceeded that observed for urban air in Beijing, China (outdoor A_{Fuchs}: ~10^2–10^3 $\mu m^2\ cm^{-3}$) (30). Our results show that the coagulation-scavenging potential of the indoor atmosphere often exceeds that of urban and forested outdoor environments during the active combustion period. Thus, determination of CoagSnk, $CoagSnk_{Net}$, and A_{Fuchs} is needed to parameterize the primary loss mechanism for indoor NCA and to elucidate factors affecting the survival of newly formed sub-3 nm molecular clusters in buildings. In contrast to $CoagSnk_{Net}$, A_{Fuchs} is computationally simple and is not a function of the Hamaker constant. As A_{Fuchs} scaled proportionally with $CoagSnk_{Net}$ (Fig. S11), A_{Fuchs} can be considered a reliable proxy for coagulation scavenging of indoor NCA.

Age-specific respiratory-tract-deposited dose rates for indoor atmospheric NCA produced during propane gas cooking

We show the evaluation of respiratory exposures to combustion-derived NCA during propane gas cooking in Fig. 5. Significant formation of indoor atmospheric NCA during propane gas cooking

resulted in large cumulative respiratory-tract-deposited doses (D_{NCA}) of NCA in the head airways and tracheobronchial region (Figs. 1, 4, and 5). During a 20-min propane cooking period, D_{NCA} ranged from about 10 billion to 1 trillion deposited NCA in the adult respiratory system (Fig. 1), with much of this dose attributed to sub-1.5 nm NCA (Fig. 5). D_{NCA} was greater for small/moderate indoor CoagSnk cases compared with large indoor CoagSnk cases due to enhanced intermodal coagulation scavenging of NCA in the latter. Size-integrated indoor NCA dose rates ($R_{D,NCA}$) were one to two orders of magnitude greater than what one would receive due to inhalation of traffic-associated NCA in the outdoor environment (2) (Fig. 4). Such substantial doses and dose rates of indoor NCA from propane gas cooking are of concern, given the toxicity of flame-generated NCA (13–15) and widespread use of gas combustion in residential indoor spaces among the global population (25–27). Future field measurements of indoor atmospheric NCA down to 1 nm will help to establish relationships between NCA exposures and respiratory health outcomes.

To investigate differences in the respiratory burden of combustion-derived NCA among children and adults, we determined age-specific weight-normalized NCA dose rates, expressed as $dR_D/dlogD_p$ ($min^{-1}\ kg^{-1}$) (Fig. 5). $dR_D/dlogD_p$ increased with decreasing diameter for both age groups, demonstrating the importance of accurate size classification and detection of NCA from 1 to 3 nm. Sub-1.5 nm weight-normalized NCA dose rates ranged from 10^8 to $10^{11}\ min^{-1}\ kg^{-1}$ (Fig. 5). For both children and adults, the largest NCA dose was received in the head airways, followed by the tracheobronchial region, and then the pulmonary region (Fig. 5); this finding is consistent with the relative magnitude of the size-resolved deposition fraction curves for each respiratory tract region (Fig. S7). We found children to have higher weight-normalized NCA dose rates compared with adults ($P < 0.05$). The weight-normalized $R_{D,NCA}$ for children was greater than that for adults by about 2.3-fold for the head airways, 2.2-fold for the tracheobronchial region, and 3.0-fold for the pulmonary region. These results are important given the documented associations between the use of indoor gas combustion and childhood asthma (47), as well as evidence suggesting that gas cooking may increase the risk of respiratory symptoms in European adults (48). Weight-normalized $R_{D,NCA}$ kernel density functions for both age groups across all propane-gas-cooking measurements exhibited a unique bimodal distribution that is characterized by a higher value mode associated with small/moderate indoor CoagSnk cases and a lower value mode associated with large indoor CoagSnk cases (Fig. 5). This result illustrates the important linkage between NCA transformations and respiratory exposures, whereby accelerated NCA scavenging by larger atmospheric aerosol particles can reduce NCA doses.

Measurement uncertainties

The time evolution of the particle number size distributions for all 12 experiments in this measurement campaign (Fig. S14) suggests experiment-to-experiment variability within the same experimental category. This is expected, as realistic cooking experiments were performed in a full-scale test house (49). However, despite the variability within each category, our results clearly show the suppression of NCA during the propane-gas-cooking period for experiments with large coagulation sinks (Fig. S14, right column). To further reinforce this observation, the size-integrated NCA number concentrations are compared between small/moderate coagulation sink and large coagulation sink experiments in Fig. S10. A one-tailed right t test was performed separately for these groups, assuming the null hypothesis that there is no significant difference in the mean-size-integrated NCA number concentrations between the small/moderate and large coagulation sink experiments during propane gas cooking. The alternative hypothesis holds that the mean-size-integrated NCA number concentration during propane gas cooking is higher in small/moderate coagulation sink experiments compared with large coagulation sink experiments. This was evaluated at a 95% CI.

The t tests indicate that there is no significant difference in the mean-size-integrated NCA number concentrations between the small/moderate and large coagulation sink experiments during the first 6 min of propane gas cooking ($P = 0.0619$). However, after 6 min and until the end of the cooking period, the t tests indicate that the mean-size-integrated NCA number concentrations are significantly higher in the small/moderate coagulation sink experiments compared with the large coagulation sink experiments ($P = 10^{-5}$). Thus, Fig. S10 and the results of the t tests between the experiments with small/moderate and large coagulation sinks show that although there is variability in the experiments within the same category, as is inherent in full-scale realistic experiments, our PSMPS measurements demonstrate that propane-gas-combustion-emitted NCA during indoor cooking are inversely correlated with the coagulation potential of the indoor atmosphere.

There are also measurement uncertainties associated with the PSMPS instrument used for monitoring indoor NCA. The particle size magnifier in the PSMPS uses diethylene glycol to activate NCA; this process can be sensitive to NCA composition (50). Additionally, the charger ions generated in the soft X-ray neutralizer serve as another source of uncertainty in our measurements. We have used a data-driven charger ion correction method for our analysis (as detailed in the supplementary material). However, this method is not perfect, and the results presented in this analysis are sensitive to the charger ion correction. For example, the sub-1.5 nm particle number size distributions obtained after turning off the gas stove, as shown in Fig. 1A, are elevated due to the charger ions. The elevations in particle number size distributions observed after turning off the gas stove can be attributed to charger ions, as they disappear when the charger ion correction threshold is increased to the 99th percentile (Fig. S15). Even at the 99th percentile threshold, the plot distinctly shows particles during the active combustion period down to 1.18 nm. Considering the errors in size-integrated number concentrations between these two thresholds, there is an uncertainty of ~48% in the sub-1.5 nm size bins and ~2% in the 1.5–3 nm size bins in our measurements. This represents the maximum uncertainty, as the 99th percentile is a very conservative threshold.

Finally, while modeling $E_{NCA,app}$, there is uncertainty associated with the Hamaker constant values used in the calculation of the coagulation parameters. In the boiling water experiments, where no condensational growth is expected, we adjusted the Hamaker constant values to obtain the best agreement for the coagulation growth rate obtained from the intramodal coagulation growth model (51) and from the mode-fitting method (45). The best-fit Hamaker constant was then used for the $E_{NCA,app}$ computations in the boiling water measurements. This method is a novel approach to estimate the Hamaker constant for aerosol processes primarily driven by coagulation. However, for butter-based cooking experiments, this method was not suitable due to the condensation of low-volatility organic vapors. Thus, we performed a sensitivity analysis for both $CoagSnk_{Net}$ and $E_{NCA,app}$ (Tables S4 and S5) in the butter-based cooking experiments; the uncertainties are <20%. For the calculation of emission factors using CO_2 data, the uncertainty in the emission factor calculation is <10% (20).

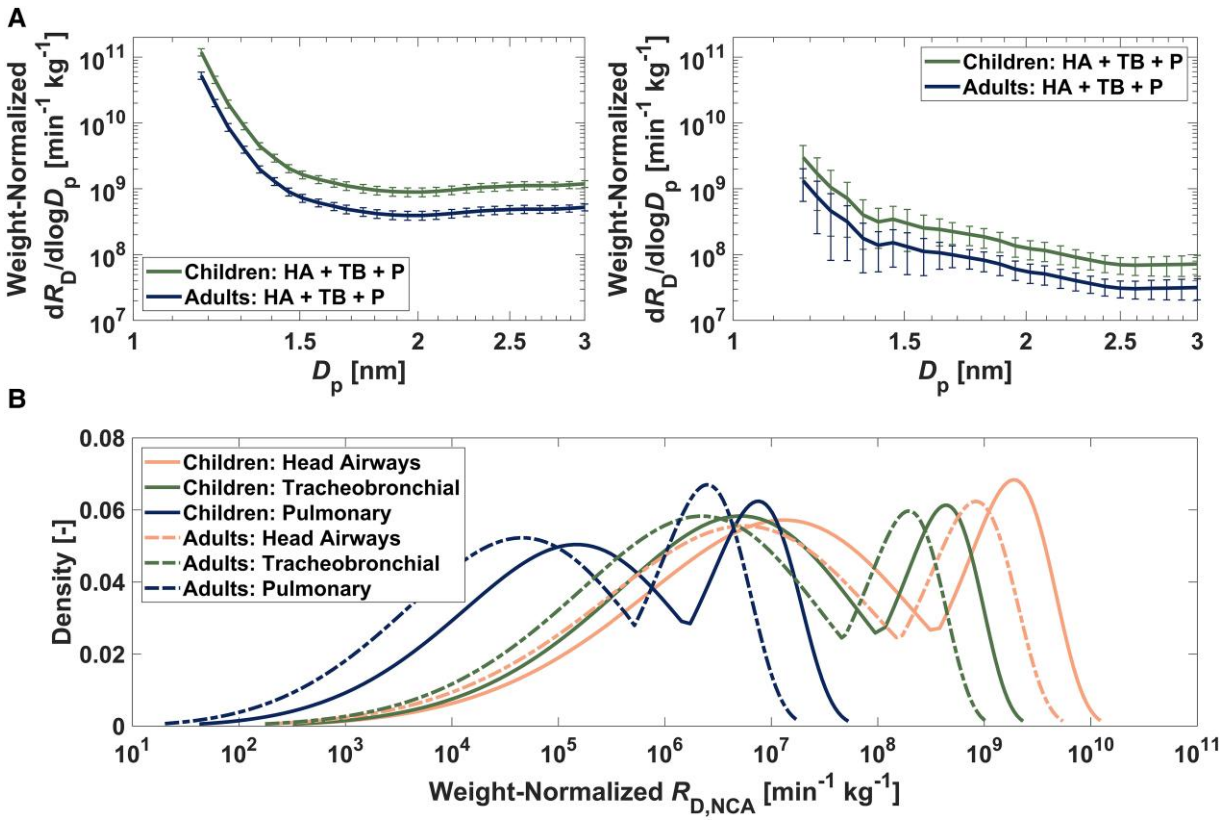

Fig. 5. Evaluation of respiratory exposures to combustion-derived NCA during propane gas cooking: A) Mean weight-normalized, size-resolved NCA respiratory-tract-deposited dose rates ($dR_D/dlogD_p$) for children and adults during propane gas cooking for (left) small/moderate indoor CoagSnk cases and (right) large indoor CoagSnk cases. The error bars represent the standard errors across all measurements. B) Kernel density functions of weight-normalized, size-integrated (1.18–3 nm) NCA respiratory-tract-deposited dose rates ($R_{D,NCA}$) for children and adults. The dose rates are apportioned by the respiratory tract region. The dose rates were calculated for each data point during the active propane-gas-combustion period of the measurements.

Materials and methods

Overview of the field measurement campaign in the Purdue zEDGE test house

Field measurements of the formation and transformation of indoor atmospheric NCA were conducted in a residential building —the Purdue zero Energy Design Guidance for Engineers (zEDGE) test house (52–56), as detailed in the supplementary material. We investigated NCA production during propane gas cooking, as discussed in the supplementary material. The indoor air mixing conditions of the test house were evaluated using four co-located battery-powered diffusion chargers (Model Pegasor AQ Indoor, Pegasor Oy, Tampere, Finland) (Fig. S3). Propane-gas-cooking experiments started at time zero, with two experimenters entering the Purdue zEDGE test house. During the initial 10 min, no activities were performed in the test house in order to establish a baseline concentration of indoor air pollutants with people present. At the 10-min mark, the propane gas stove was ignited using an electronic handheld lighter. The cooking process, as detailed in the supplementary material, was then carried out for the following 20 min. At the 30-min mark, the propane gas stove was shut down, and the experimenters exited the test house carrying the prepared food. Finally, we observed a decay in the emitted air pollutants in the unoccupied test house over a period from 30 to 150 min. The test house was operated at a nominal outdoor air ventilation rate (0.45 h^{-1}) typical of residential environments (Table S1). Similar to the HOMEChem field campaign (49), a kitchen vent hood was not operational during the measurements to represent their infrequent use in the United States (57).

High-resolution online nanoparticle measurements

Indoor atmospheric NCA number concentrations and size distributions from 1.18 to 3 nm were measured in real-time using a novel particle size magnifier—scanning mobility particle sizer (PSMPS; GRIMM Aerosol Technik Ainring GmbH & Co. KG, Ainring, Germany). The PSMPS is configured with a soft X-ray neutralizer, a Vienna-type modified short-DMA (S-DMA), a diethylene glycol-based PSM (Model A10, Airmodus Ltd., Helsinki, Finland), and a butanol-based condensation particle counter. NCA number concentrations were corrected for the presence of charger ions and diffusional losses within the PSMPS, as discussed in the supplementary material. Larger particles were measured using a SMPS with a long-DMA (Model 3938NL88, TSI Inc., Shoreview, MN, USA) and a wideband integrated bioaerosol sensor (WIBS; Model WIBS-NEO, Droplet Measurement Technologies LLC, Longmont, CO, USA).

The PSMPS, SMPS, and WIBS measured particle number size distributions ($dN/dlogD_p$; cm^{-3}) for particles from 1.18 to 55.7 nm (electrical mobility diameter), 13.1 to 572.5 nm (electrical mobility diameter), and 500 to 30,000 nm (optical equivalent diameter), respectively. The particle number size distributions from the PSMPS and SMPS in the overlapping size range (13.1 to 55.7 nm) showed reasonable agreement (Fig. S16) and were

merged using a moving average smoothing approach. A continuous, wide size-range particle number size distribution was obtained, spanning from 1.18 to 30,000 nm. This included PSMPS data alone from 1.18 to 13.1 nm, moving average merged data from the PSMPS and SMPS from 13.1 to 55.7 nm, SMPS data from 55.7 to 500 nm, and WIBS data from 500 to 30,000 nm. Details about the data analysis are available in the supplementary material. NCA number concentrations (N_{NCA}; cm^{-3}) were calculated by size-integrating the particle number size distributions from 1.18 to 3 nm. The merged particle number size distributions ($dN/dlogD_p$; cm^{-3}) were converted to particle surface area size distributions ($dS/dlogD_p$; $\mu m^2\ cm^{-3}$) assuming spherical particles (dynamic shape factor: $\chi = 1$) and particle mass size distributions ($dM/dlogD_p$; $\mu g\ m^{-3}$) assuming the particle effective densities listed in Table S2. The particle mass size distributions were then size-integrated from 1.18 to 2,500 nm to obtain $PM_{2.5}$ mass concentrations ($\mu g\ m^{-3}$) (58).

Other air quality instrumentation used during the field measurement campaign included a NO_x (NO and NO_2) analyzer (Model 42C, Thermo Electron Corp., Waltham, MA, USA), a CO_2 analyzer (Model LI-830, LI-COR Biosciences, Lincoln, NE, USA), and a handheld humidity and temperature meter (Model HM70, Vaisala Oyj, Helsinki, Finland).

Size-resolved indoor atmospheric NCA dynamics model

To facilitate generalization of the combustion-derived NCA results to different indoor atmospheric environments, the size-integrated indoor atmospheric apparent NCA emission rate ($E_{NCA,app}$; min^{-1}) was estimated from the discrete aerosol GDE (28, 29) as shown in Eq. 1:

$$E_{NCA,app} = V \times \sum_{d_p=1.18\,nm}^{d_p=3\,nm} \left(\frac{dN_{d_{p,i}}}{dt} + \text{Ventilation loss} + \text{Deposition loss} + \text{Coagulation loss} + \text{Condensation loss} - \text{Coagulation source} - \text{Condensation source} \right) \quad (1)$$

Expanding each term in Eq. 1, $E_{NCA,app}$ can be written (as described in the supplementary material) as shown in Eq. 2:

$$E_{NCA,app} = V \times \sum_{d_p=1.18\,nm}^{d_p=3\,nm} \left(\frac{dN_{d_{p,i}}}{dt} + k_{vent} \times N_{d_{p,i}} + k_{dep,d_p} \times N_{d_{p,i}} + \text{CoagSnk}_{d_p} \times N_{d_{p,i}} - \text{CoagSrc}_{d_p} + \text{Cond}_{d_{p,i}} - \text{Cond}_{(d_{p,i-1})} \right) \quad (2)$$

where V is the well-mixed interior volume of the Purdue zEDGE test house (cm^3) and $N_{d_{p,i}}$ is the number concentration (cm^{-3}) in size bin i. All particles in a size bin i are characterized by the midpoint diameter, d_p, which represents the average diameter between the boundaries of the bin. Table S8 provides the bin boundaries and the midpoint diameters of the NCA size bins of the PSMPS. $dN_{d_{p,i}}/dt$ is the time derivative of $N_{d_{p,i}}$ ($cm^{-3}\ min^{-1}$); k_{vent} is the outdoor air ventilation rate (min^{-1}); k_{dep,d_p} is the size-dependent first-order deposition loss rate coefficient of particles at size d_p (min^{-1}); CoagSnk_{d_p} is the coagulation sink of particles at size d_p (min^{-1}); and CoagSrc_{d_p} is the coagulation source of particles at size d_p ($cm^{-3}\ min^{-1}$). The coagulation sink (CoagSnk_{d_p}) is the rate at which particles at size d_p are scavenged due to coagulation, and is calculated as shown in Eq. 3:

$$\text{CoagSnk}_{d_p} = \sum_{d'_p=1.18\,nm}^{d'_p=2,500\,nm} k_{coag}(d_p, d'_p) \times N_{d'_{p,i}} \quad (3)$$

where $k_{coag}(d_p, d'_p)$ is the coagulation coefficient between particles at sizes d_p and d'_p ($cm^3\ min^{-1}$), and is obtained using the Brownian and van der Waals viscous forces coagulation model (59), and $N_{d'_{p,i}}$ is the number concentration in size bin i with midpoint diameter d'_p. The formation of particles due to coagulation among smaller particles (CoagSrc_{d_p}) is expressed as shown in Eq. 4:

$$\text{CoagSrc}_{d_p} = \sum_{d_p^3 = d'^3_p + d''^3_p}^{d'_p,\ d''_p < d_p} 0.5 \times k_{coag}(d'_p, d''_p) \times N_{d'_{p,i}} \times N_{d''_{p,j}} \quad (4)$$

where d'_p and d''_p are particles with sizes smaller than d_p which coagulate to form particles at size d_p, and $N_{d'_p}$ and $N_{d''_p}$ are the corresponding number concentrations in size bins i and j with midpoint diameters d'_p and d''_p, respectively. Since the smallest bin in which the PSMPS can detect particles is characterized by $d_p = 1.18$ nm, the lower limit of the coagulation source term that can be factored in is derived from the self-coagulation of particles in the smallest detectable size bin, resulting in particles at size $d_p = 1.46$ nm. Thus, the coagulation source is only computed for particles at sizes >1.46 nm, and thus, the computation of apparent emission rates for sizes <1.46 nm does not feature the coagulation source term.

The net difference between CoagSnk_{d_p} and CoagSrc_{d_p}, represented as $\text{CoagSnk}_{Net,d_p}$ (min^{-1}), effectively captures the coagulation scavenging effect of particles at size d_p (29). $\text{CoagSnk}_{Net,d_p}$ is calculated as shown in Eq. 5:

$$\text{CoagSnk}_{Net,d_p} = \text{CoagSnk}_{d_p} - \frac{\text{CoagSrc}_{d_p}}{N_{d_{p,i}}} \quad (5)$$

In this study, CoagSnk_{Net} represents the median value of $\text{CoagSnk}_{Net,d_p}$ for 1.18 nm $< d_p <$ 3 nm. In addition to CoagSnk_{Net}, the effect of coagulation scavenging was parametrized by the aerosol Fuchs surface area (A_{Fuchs}; $\mu m^2\ cm^{-3}$), calculated as shown in Eq. 6:

$$A_{Fuchs} = \frac{4\pi}{3} \int_{d_p=1.18\,nm}^{d_p=2,500\,nm} d_p^2 \times \left(\frac{Kn + Kn^2}{1 + 1.71Kn + 1.33Kn^2} \right) \times \frac{dN}{dlogD_p} dlogD_p \quad (6)$$

where Kn is the particle Knudsen number.

The condensation loss of particles at size d_p is the condensational particle flux from the size bin i, with midpoint diameter d_p, to the next size bin due to the condensation of low-volatility cooking vapors (32). This is parametrized as shown in Eq. 7:

$$\text{Cond}_{d_{p,i}} = \frac{GR_{d_p}}{\Delta d_{p,i}} \times N_{d_{p,i}} \quad (7)$$

Similarly, the condensation source of particles in a size bin i, with midpoint diameter d_p, is the condensational particle flux from the previous size bin ($\text{Cond}_{(d_{p,i-1})}$). In Eq. 7, $\Delta d_{p,i}$ is the width of the size bin i and GR_{d_p} is the net condensational growth rate of particles at size d_p (GR_{Cond,d_p}; nm min^{-1}), calculated using the mode-fitting method and is corrected for the growth rate due to intramodal coagulation (GR_{Coag,d_p}; nm min^{-1}) and intermodal coagulation (GR_{Scav,d_p}; nm min^{-1}) (45), as detailed in the supplementary material. Condensational particle growth is considered only in butter-based cooking experiments (buttermilk pancakes and grilled cheese) due to the

emissions of low-volatility cooking vapors (44). However, in the boiling water experiments, condensational growth is ignored because of the absence of a low-volatility vapor source and the nonhygroscopic nature of freshly nucleated soot particles (60) in the observed RH range (Fig. S17).

Additionally, the particle number size distributions ($dN/d\log D_p$; cm^{-3}) and the size-integrated NCA number concentrations (N_{NCA}; cm^{-3}) were converted into emission factors using Eq. 8 as follows (20):

$$E_X = \frac{\Delta X}{\Delta CO_2} \times \frac{MW_{CO_2}}{AW_C} \times C_f \times 10^{15} \quad (8)$$

where ΔX is the background corrected particle number size distributions or size-integrated NCA number concentrations; ΔCO_2 is the background corrected CO_2 concentration in the test house in $\mu g\ m^{-3}$; MW_{CO_2} and AW_C are the molecular weight of CO_2 and atomic weight of carbon, respectively; and C_f is the mass fraction of carbon in the propane fuel (assumed as 0.85 g kg-fuel^{-1} (20)). Additional details on this formulation are provided in the supplementary material.

Finally, age-specific size-resolved respiratory-tract-deposited dose rates ($dR_D/d\log D_p$; min^{-1}) for propane-gas-stove-cooking-emitted NCA were estimated as shown in Eq. 9:

$$\frac{dR_D}{d\log D_p} = Q \times DF_{d_p} \times \frac{dN}{d\log D_p} \quad (9)$$

where Q is the inhalation rate ($m^3\ min^{-1}$) and DF_{d_p} is the size-resolved deposition fraction of particles in each respiratory tract region (head airways, tracheobronchial, pulmonary), as detailed in the supplementary material. $dR_D/d\log D_p$ was size integrated from 1.18 to 3 nm to obtain the NCA respiratory-tract-deposited dose rate ($R_{D,NCA}$; min^{-1}), and further integrated over time to obtain the cumulative respiratory-tract-deposited dose (D_{NCA}). The dose-rate parameters were then normalized by the body weights of children and adults as $min^{-1}\ kg^{-1}$ (61), as detailed in the supplementary material.

Supplementary Material

Supplementary material is available at *PNAS Nexus* online.

Funding

Financial support was provided by the National Science Foundation (CBET-1847493 to B.E.B.), the Alfred P. Sloan Foundation Chemistry of the Indoor Environments Program (G-2018-11061 to B.E.B. and P.S.), Purdue University start-up funds (to N.J.), and the Purdue University Libraries Open Access Publishing Fund (to B.E.B.).

Author Contributions

B.E.B., N.J., and P.S. designed the research study. S.S.P., J.J., X.D., C.H., E.K.R., V.K., P.P., P.S., N.J., and B.E.B. conducted the research study and collected the data. C.K. and G.S. contributed new analytic tools. S.S.P., N.J., and B.E.B. analyzed the data. S.S.P., N.J., and B.E.B. wrote the manuscript with input from all coauthors. B.E.B. managed the research study.

Data Availability

All data are included in the manuscript and/or supplementary material.

References

1 Rosales CMF, *et al.* 2022. Chemistry and human exposure implications of secondary organic aerosol production from indoor terpene ozonolysis. *Sci Adv*. 8:eabj9156.
2 Rönkkö T, *et al.* 2017. Traffic is a major source of atmospheric nanocluster aerosol. *Proc Natl Acad Sci U S A*. 114:7549–7554.
3 Kontkanen J, *et al.* 2017. Measurements of sub-3 nm particles using a particle size magnifier in different environments: from clean mountain top to polluted megacities. *Atmos Chem Phys*. 17:2163–2187.
4 Kangasluoma J, Kontkanen J. 2017. On the sources of uncertainty in the sub-3 nm particle concentration measurement. *J Aerosol Sci*. 112:34–51.
5 Stolzenburg D, Steiner G, Winkler PM. 2017. A DMA-train for precision measurement of sub-10 nm aerosol dynamics. *Atmos Meas Tech*. 10:1639–1651.
6 Deng C, Cai R, Yan C, Zheng J, Jiang J. 2021. Formation and growth of sub-3 nm particles in megacities: impact of background aerosols. *Faraday Discuss*. 226:348–363.
7 Deng C, *et al.* 2020. Seasonal characteristics of new particle formation and growth in urban Beijing. *Environ Sci Technol*. 54:8547–8557.
8 Garcia GJM, Schroeter JD, Kimbell JS. 2015. Olfactory deposition of inhaled nanoparticles in humans. *Inhal Toxicol*. 27:394–403.
9 Kreyling WG, *et al.* 2014. Air–blood barrier translocation of tracheally instilled gold nanoparticles inversely depends on particle size. *ACS Nano*. 8:222–233.
10 Oberdörster G, *et al.* 2004. Translocation of inhaled ultrafine particles to the brain. *Inhal Toxicol*. 16:437–445.
11 Peters A, Rückerl R, Cyrys J. 2011. Lessons from air pollution epidemiology for studies of engineered nanomaterials. *J Occup Environ Med*. 53:S8–S13.
12 Pedata P, *et al.* 2015. "Are we forgetting the smallest, sub 10 nm combustion generated particles?". *Part Fibre Toxicol*. 12:34.
13 Sgro LA, *et al.* 2009. Toxicological properties of nanoparticles of organic compounds (NOC) from flames and vehicle exhausts. *Environ Sci Technol*. 43:2608–2613.
14 Pedata P, *et al.* 2013. Apoptotic and proinflammatory effect of combustion-generated organic nanoparticles in endothelial cells. *Toxicol Lett*. 219:307–314.
15 Pedata P, *et al.* 2012. Interaction between combustion-generated organic nanoparticles and biological systems: in vitro study of cell toxicity and apoptosis in human keratinocytes. *Nanotoxicology*. 6:338–352.
16 Patra SS, Ramsisaria R, Du R, Wu T, Boor BE. 2021. A machine learning field calibration method for improving the performance of low-cost particle sensors. *Build Environ*. 190:107457.
17 Jeong S-G, Wallace L, Rim D. 2021. Contributions of coagulation, deposition, and ventilation to the removal of airborne nanoparticles in indoor environments. *Environ Sci Technol*. 55:9730–9739.
18 Yang S, *et al.* 2021. Ozone initiates human-derived emission of nanocluster aerosols. *Environ Sci Technol*. 55:14536–14545.
19 Poikkimäki M, *et al.* 2019. Nanocluster aerosol emissions of a 3D printer. *Environ Sci Technol*. 53:13618–13628.
20 Jathar SH, *et al.* 2020. Emissions and radiative impacts of sub-10 nm particles from biofuel and fossil fuel cookstoves. *Aerosol Sci Technol*. 54:1231–1243.
21 Patel S, *et al.* 2020. Indoor particulate matter during HOMEChem: concentrations, size distributions, and exposures. *Environ Sci Technol*. 54:7107–7116.
22 D'Anna A. 2009. Combustion-formed nanoparticles. *Proc Combust Inst*. 32:593–613.

23 Zimmerman A, Petters MD, Meskhidze N. 2020. Observations of new particle formation, modal growth rates, and direct emissions of sub-10 nm particles in an urban environment. *Atmos Environ*. 242:117835.

24 Caracci E, Canale L, Buonanno G, Stabile L. 2022. Sub-micron particle number emission from residential heating systems: a comparison between conventional and condensing boilers fueled by natural gas and liquid petroleum gas, and pellet stoves. *Sci Total Environ*. 827:154288.

25 Beall R. 2022. In 2020, most U.S. households prepared at least one hot meal a day at home. U.S. Energy Information Administration (EIA) [accessed date 2023 Jul 8]. https://www.eia.gov/todayinenergy/detail.php?id=53439#:~:text=In%202020%2C%2079%25%20of%20U.S.,hot%20meals%20at%20home%20daily.

26 Chadwick L. 2023. Scientists say gas stoves can emit chemical linked to cancer at levels higher than second-hand smoke. Euronews [accessed date 2023 Jul 8]. https://www.euronews.com/health/2023/06/19/gas-stoves-can-emit-chemical-linked-to-cancer-at-higher-levels-than-second-hand-tobacco-sm?utm_source=Linkedin&utm_medium=Social.

27 Stoner O, *et al.* 2021. Household cooking fuel estimates at global and country level for 1990 to 2030. *Nat Commun*. 12:5793.

28 Kulmala M, *et al.* 2012. Measurement of the nucleation of atmospheric aerosol particles. *Nat Protoc*. 7:1651–1667.

29 Cai R, Jiang J. 2017. A new balance formula to estimate new particle formation rate: reevaluating the effect of coagulation scavenging. *Atmos Chem Phys*. 17:12659–12675.

30 Cai R, *et al.* 2017. Aerosol surface area concentration: a governing factor in new particle formation in Beijing. *Atmos Chem Phys*. 17:12327–12340.

31 Gong Y, *et al.* 2010. Competition of coagulation sink and source rate: new particle formation in the Pearl River Delta of China. *Atmos Environ*. 44:3278–3285.

32 Dal Maso M, *et al.* 2002. Condensation and coagulation sinks and formation of nucleation mode particles in coastal and boreal forest boundary layers. *J Geophys Res Atmos*. 107:PAR 2-1–PAR 2-10.

33 Tang Q, Cai R, You X, Jiang J. 2017. Nascent soot particle size distributions down to 1 nm from a laminar premixed burner-stabilized stagnation ethylene flame. *Proc Combust Inst*. 36:993–1000.

34 Johansson KO, El Gabaly F, Schrader PE, Campbell MF, Michelsen HA. 2017. Evolution of maturity levels of the particle surface and bulk during soot growth and oxidation in a flame. *Aerosol Sci Technol*. 51:1333–1344.

35 D'Anna A, Sirignano M, Kent J. 2010. A model of particle nucleation in premixed ethylene flames. *Combust Flame*. 157:2106–2115.

36 Abid AD, *et al.* 2009. Size distribution and morphology of nascent soot in premixed ethylene flames with and without benzene doping. *Proc Combust Inst*. 32:681–688.

37 Martin JW, Salamanca M, Kraft M. 2022. Soot inception: carbonaceous nanoparticle formation in flames. *Prog Energy Combust Sci*. 88:100956.

38 D'Anna A, Commodo M, Violi S, Allouis C, Kent J. 2007. Nano organic carbon and soot in turbulent non-premixed ethylene flames. *Proc Combust Inst*. 31:621–629.

39 D'Anna A, Rolando A, Allouis C, Minutolo P, D'Alessio A. 2005. Nano-organic carbon and soot particle measurements in a laminar ethylene diffusion flame. *Proc Combust Inst*. 30:1449–1456.

40 Cai R, *et al.* 2022. Survival probability of new atmospheric particles: closure between theory and measurements from 1.4 to 100 nm. *Atmos Chem Phys*. 22:14571–14587.

41 Jacobson MZ, Seinfeld JH. 2004. Evolution of nanoparticle size and mixing state near the point of emission. *Atmos Environ*. 38:1839–1850.

42 Yu F. 2001. Chemiions and nanoparticle formation in diesel engine exhaust. *Geophys Res Lett*. 28:4191–4194.

43 Cummings BE, *et al.* 2023. Model framework for predicting semivolatile organic material emissions indoors from organic aerosol measurements: applications to HOMEChem stir-frying. *Environ Sci Technol*. 57:17374–17383.

44 Masoud CG, *et al.* 2022. Molecular composition and gas-particle partitioning of indoor cooking aerosol: insights from a FIGAERO-CIMS and kinetic aerosol modeling. *Aerosol Sci Technol*. 56:1156–1173.

45 Stolzenburg D, *et al.* 2023. Atmospheric nanoparticle growth. *Rev Mod Phys*. 95:45002.

46 Gren L, *et al.* 2021. Effects of renewable fuel and exhaust aftertreatment on primary and secondary emissions from a modern heavy-duty diesel engine. *J Aerosol Sci*. 156:105781.

47 Gruenwald T, Seals BA, Knibbs LD, Hosgood HD III. 2022. Population attributable fraction of gas stoves and childhood asthma in the United States. *Int J Environ Res Public Health*. 20:75.

48 Pan H, *et al.* 2024. Gas cooking indoors and respiratory symptoms in the ECRHS cohort. *Int J Hyg Environ Health*. 256:114310.

49 Farmer DK, *et al.* 2019. Overview of HOMEChem: house observations of microbial and environmental chemistry. *Environ Sci Processes Impacts*. 21:1280–1300.

50 Kangasluoma J, *et al.* 2020. Overview of measurements and current instrumentation for 1–10 nm aerosol particle number size distributions. *J Aerosol Sci*. 148:105584.

51 Cai R, *et al.* 2021. Impacts of coagulation on the appearance time method for new particle growth rate evaluation and their corrections. *Atmos Chem Phys*. 21:2287–2304.

52 Ding X, *et al.* 2023. Evaluation of workplace exposures to volatile chemicals during COVID-19 building disinfection activities with proton transfer reaction mass spectrometry. *Ann Work Expo Health*. 67:546–551.

53 Jiang J, *et al.* 2021. Real-time measurements of botanical disinfectant emissions, transformations, and multiphase inhalation exposures in buildings. *Environ Sci Technol Lett*. 8:558–566.

54 Jiang J, *et al.* 2021. Ethanol-based disinfectant sprays drive rapid changes in the chemical composition of indoor air in residential buildings. *J Hazard Mater Lett*. 2:100042.

55 Jiang J, *et al.* 2023. Siloxane emissions and exposures during the use of hair care products in buildings. *Environ Sci Technol*. 57:19999–20009.

56 Ding X, *et al.* 2023. Real-time indoor sensing of volatile organic compounds during building disinfection events via photoionization detection and proton transfer reaction mass spectrometry. *Build Environ*. 246:110953.

57 Zhao H, *et al.* 2020. Factors impacting range hood use in California houses and low-income apartments. *Int J Environ Res Public Health*. 17:8870.

58 Patra SS, Wu T, Wagner DN, Jiang J, Boor BE. 2021. Real-time measurements of fluorescent aerosol particles in a living laboratory office under variable human occupancy and ventilation conditions. *Build Environ*. 205:108249.

59 Rim D, Choi J-I, Wallace LA. 2016. Size-resolved source emission rates of indoor ultrafine particles considering coagulation. *Environ Sci Technol*. 50:10031–10038.

60 Zhang R, *et al.* 2008. Variability in morphology, hygroscopicity, and optical properties of soot aerosols during atmospheric processing. *Proc Natl Acad Sci U S A*. 105:10291–10296.

61 Wu T, *et al.* 2018. Infant and adult inhalation exposure to resuspended biological particulate matter. *Environ Sci Technol*. 52:237–247.